

Cite this: *Chem. Sci.*, 2021, 12, 14660

All publication charges for this article have been paid for by the Royal Society of Chemistry

Received 8th June 2021  
Accepted 6th September 2021

DOI: 10.1039/d1sc03109k

rsc.li/chemical-science

# Tuning product selectivity in CO<sub>2</sub> hydrogenation over metal-based catalysts

Ling-Xiang Wang,<sup>a</sup> Liang Wang<sup>\*b</sup> and Feng-Shou Xiao <sup>\*b</sup>

Conversion of CO<sub>2</sub> into chemicals is a promising strategy for CO<sub>2</sub> utilization, but its intricate transformation pathways and insufficient product selectivity still pose challenges. Exploiting new catalysts for tuning product selectivity in CO<sub>2</sub> hydrogenation is important to improve the viability of this technology, where reverse water-gas shift (RWGS) and methanation as competitive reactions play key roles in controlling product selectivity in CO<sub>2</sub> hydrogenation. So far, a series of metal-based catalysts with adjustable strong metal–support interactions, metal surface structure, and local environment of active sites have been developed, significantly tuning the product selectivity in CO<sub>2</sub> hydrogenation. Herein, we describe the recent advances in the fundamental understanding of the two reactions in CO<sub>2</sub> hydrogenation, in terms of emerging new catalysts which regulate the catalytic structure and switch reaction pathways, where the strong metal–support interactions, metal surface structure, and local environment of the active sites are particularly discussed. They are expected to enable efficient catalyst design for minimizing the deep hydrogenation and controlling the reaction towards the RWGS reaction. Finally, the potential utilization of these strategies for improving the performance of industrial catalysts is examined.

## 1. Introduction

Carbon dioxide (CO<sub>2</sub>), a major greenhouse gas, has been paid much attention recently due to the consumption of massive amounts of fossil fuel and increase of atmospheric CO<sub>2</sub> level, and a solution for this challenge is to suppress CO<sub>2</sub> emission.<sup>1</sup> To this end, transformation of CO<sub>2</sub> into chemicals is extremely

promising, which not only benefits the CO<sub>2</sub> elimination but also provides carbon resources for industrial processes.<sup>2–6</sup> In these transformations, CO<sub>2</sub> hydrogenation over metal-based catalysts is a critical route, but the intricate transformation network and multiple active sites strongly influence the product selectivity.<sup>7–11</sup> In recent years, various chemicals have been achieved *via* CO<sub>2</sub> hydrogenation, including CO,<sup>12–22</sup> methane,<sup>23–27</sup> methanol,<sup>28–37</sup> olefins,<sup>38–41</sup> gasolines,<sup>42–46</sup> aromatics,<sup>47–51</sup> and alcohols.<sup>52–58</sup>

Among these products, CO formed by reverse water-gas shift (RWGS) and CH<sub>4</sub> formed by CO<sub>2</sub> methanation are the most fundamental products, which are usually chosen as model

<sup>a</sup>Department of Chemistry, Zhejiang University, Hangzhou 310028, China

<sup>b</sup>Key Lab of Biomass Chemical Engineering of Ministry of Education, College of Chemical and Biological Engineering, Zhejiang University, Hangzhou 310027, China. E-mail: fjsxiao@zju.edu.cn; liangwang@zju.edu.cn



Ling-Xiang Wang received his B.S. degree (2016) from Wuhan University, and his PhD degree (2021) in Chemistry from Zhejiang University, China. His research is mainly focused on metal/oxide catalysts toward CO<sub>2</sub> conversion.



Liang Wang received his B.S. degree (2008) in chemistry from Jilin University, China. He obtained his PhD degree from the State Key Laboratory of Inorganic Synthesis and Preparative Chemistry, Jilin University in 2013. He then joined the Institute of Catalysis in Zhejiang University for postdoctoral work. Currently, he is a research professor in the College of Chemical and Biological Engineering in Zhejiang University. His research is focused on nanoporous catalysts and the conversion of low-carbon molecules.

His research is focused on nanoporous catalysts and the conversion of low-carbon molecules.



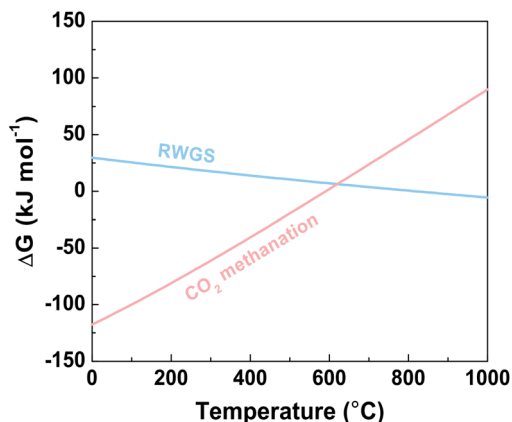
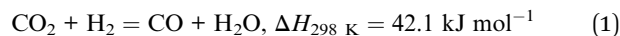


Fig. 1 Gibbs free energy of the RWGS reaction and CO<sub>2</sub> methanation.

products for investigations due to their strong competitiveness. From the viewpoint of chemical transformation, CO is preferred because of its potential for further applications, such as Fischer–Tropsch synthesis for hydrocarbons and oxygenates which possess higher economic value.<sup>59–62</sup> In contrast, methane is relatively undesirable because of the limited applications and transformation routes. On the other hand, CO is a primary product and/or intermediate, which could be further transformed into other products. In contrast, methane is the completely hydrogenated product, which is basically stable in CO<sub>2</sub> hydrogenation. Therefore, studying the selectivity control between CO and methane could provide deep understanding of reaction mechanisms of CO<sub>2</sub> hydrogenation, which should be helpful for designing highly efficient catalysts. This understanding even helps to improve the catalysis in methanol and C<sub>2+</sub> product synthesis from CO<sub>2</sub> hydrogenation.<sup>17</sup>

As shown in Fig. 1, the RWGS is thermodynamically favorable at high temperature because of its endothermic nature, while CO<sub>2</sub> methanation is thermodynamically favorable at relatively low temperature. However, the eight-electron transfer process of CO<sub>2</sub> to CH<sub>4</sub> is hindered by the high kinetic barrier. To

overcome the kinetic limitation, a large number of catalysts have been employed for efficient CO<sub>2</sub> hydrogenation.<sup>7,9,23,24</sup>



The CO<sub>2</sub>-to-CO/CH<sub>4</sub> transformation is very complex. In most cases, \*CO is an infeasible intermediate during CO<sub>2</sub> hydrogenation.<sup>9,32</sup> The CO<sub>2</sub> hydrogenation proceeds *via* primary hydrogenation to \*CO, and deep hydrogenation of \*CO to methane. Based on this knowledge, the adsorption strength of \*CO on the catalyst surface is regarded as a crucial factor (Fig. 2a). For example, Cu catalysts prefer to catalyze the RWGS reaction,<sup>34</sup> while Co and Ni catalysts are favorable for CO<sub>2</sub> methanation.<sup>24,63</sup> These results are attributed to the fact that Co and Ni exhibit stronger adsorption for the \*CO intermediate than Cu, thus leading to efficient C–O bond cleavage to form methane.<sup>9,16</sup> The surface electronic states of the supported metal nanoparticles could optimize the \*CO adsorption, which could be significantly controlled by strong metal–support interactions (SMSI) on reducible oxide supports. With the discovery of SMSI on non-oxides, the strategy of \*CO-adsorption control for tuning product selectivity in CO<sub>2</sub> hydrogenation is expanded to phosphates. Based on the transformation routes of \*CO to CH<sub>4</sub>, as far as inhibiting C–O dissociation and deep hydrogenation of \*CO species is concerned, new catalysts including bimetallic alloys and carbides are exploited (Fig. 2b). In addition, during SMSI construction, O vacancies easily form on the reducible oxide supports and play a crucial role in a series of charge transfer processes. The O vacancies could result in positively charged metal nanoparticles, which reduces the back-donation of d-electrons to the 2π antibonding orbital of CO, and the interaction between metal and \*CO species is weakened.<sup>64</sup> Based on this understanding, the advantages of alloy and carbide catalysts are maximized, because alloy catalysts have adjustable electronic structures for optimizing reaction intermediate adsorption, and carbide catalysts can provide a functional catalytic surface for new reaction routes (Fig. 2c). These unique structures and surface properties show more opportunities for selective CO<sub>2</sub> hydrogenation. In addition to \*CO-adsorption, \*H spillover on the catalytic surface is equally remarkable.<sup>9,10,28</sup> Under the precondition of moderate H<sub>2</sub> dissociation, inhibiting \*H spillover efficiently avoids deep hydrogenation of \*CO, which might provide new insights for selectivity control in CO<sub>2</sub> hydrogenation.

With regard to the rapid growth of investigations in selective CO<sub>2</sub> hydrogenation, and the requirements for in-depth understanding of reaction mechanisms, we believe that it is time to summarize recent achievements in tuning product selectivity in CO<sub>2</sub> hydrogenation. Previous reviews have focused on applications of the catalysts and the reaction mechanisms from CO<sub>2</sub> to specific products,<sup>7–10,65,66</sup> but strategies for selectivity control and principles for catalyst design are rarely discussed. In this perspective, the structural features of oxide, phosphate, metal alloy, and carbide-based catalysts are briefly summarized.



Prof. Feng-Shou Xiao received his B.S. and M.S. degrees in chemistry from Jilin University, China. From there he moved to the Catalysis Research Center, Hokkaido University, Japan, where he was involved in collaborative research between China and Japan. He was awarded his PhD degree at Jilin University in 1990. After postdoctoral work at the University of California at Davis, USA, he joined Jilin University in

1994, where he is a distinguished professor of chemistry. He moved to Zhejiang University in 2009, and is now a distinguished professor at the College of Chemical and Biological Engineering. His research is mainly focused on zeolites, porous materials, and catalysis.



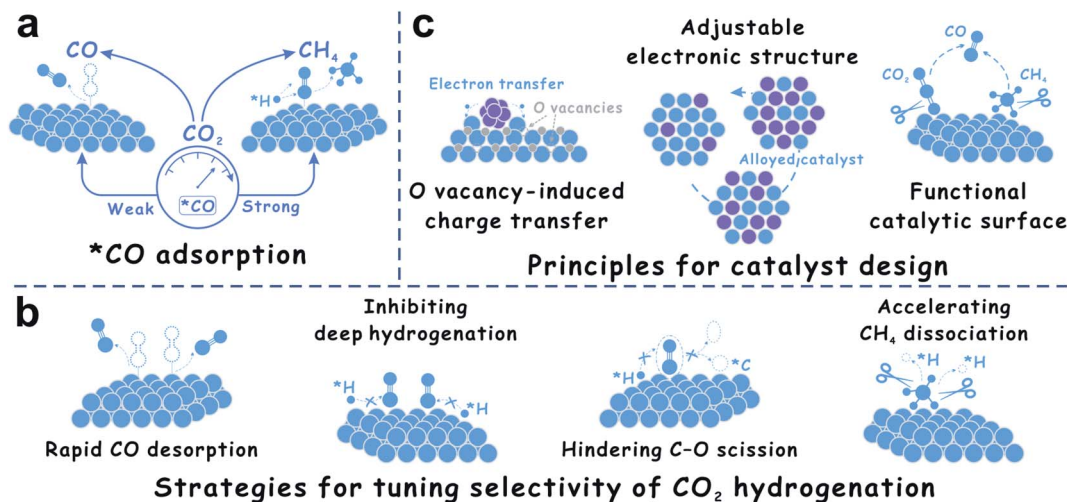


Fig. 2 (a) Importance of  $^*CO$  adsorption in  $CO_2$  hydrogenation. (b) Strategies for tuning the selectivity of  $CO_2$  hydrogenation. (c) Principles for catalyst design for  $CO_2$  hydrogenation.

Furthermore, the principles for controlling the product selectivity are proposed.

## 2. Oxide-supported metal nanoparticle catalysts

### 2.1 Crystal phase of oxides

A typical phenomenon is observed on titania-supported cobalt catalysts,<sup>67–69</sup> where Co/r-TiO<sub>2</sub> (rutile) selectively catalyzes  $CO_2$  methanation, but CO is predominant on the Co/a-TiO<sub>2</sub> (anatase) catalyst.<sup>69</sup> Calcination at 800 °C results in a partial transition from anatase to rutile, enhancing the adsorption of the  $^*CO$  intermediate that leads to deep hydrogenation to  $CH_4$ .<sup>16,34,70,71</sup> Similarly, CO selectivity in In<sub>2</sub>O<sub>3</sub> catalyzed  $CO_2$  hydrogenation can be improved by crystal phase transition from hexagonal In<sub>2</sub>O<sub>3</sub> (h-In<sub>2</sub>O<sub>3</sub>) to cubic In<sub>2</sub>O<sub>3</sub> (c-In<sub>2</sub>O<sub>3</sub>).<sup>72</sup> The h-In<sub>2</sub>O<sub>3</sub> is reduced by H<sub>2</sub> and oxidized by CO<sub>2</sub> to form c-In<sub>2</sub>O<sub>3</sub>. The rearrangement of surface O species makes it more active for H<sub>2</sub> dissociation to form O vacancies. CO<sub>2</sub> adsorbs on the O vacancies and heals the vacancies by desorbing CO, resulting in higher RWGS activity.<sup>73–76</sup> Yang *et al.*<sup>17</sup> reported the transformation from Co<sub>3</sub>O<sub>4</sub> rhombic dodecahedra (denoted as Co<sub>3</sub>O<sub>4</sub>-0 h) with the (111) plane to Co<sub>3</sub>O<sub>4</sub> nanorods (Co<sub>3</sub>O<sub>4</sub>-2 h) with the (110) plane by prolonging hydrothermal aging during synthesis, leading to different catalytic performances. For example, CO selectivity of Co<sub>3</sub>O<sub>4</sub>-2 h exceeds 90%, while the catalyst without aging (Co<sub>3</sub>O<sub>4</sub>-0 h) gives a CH<sub>4</sub> selectivity of 85% in  $CO_2$  hydrogenation. Density functional theory (DFT) calculations reveal that the formation of O vacancies on Co<sub>3</sub>O<sub>4</sub>(111) (0.96 eV) is much easier than that on the Co<sub>3</sub>O<sub>4</sub>(110) surface (2.20–2.79 eV). The O vacancies lead to low-coordinated Co atoms, followed by the formation of a metallic Co cluster, which is highly active for  $CO_2$  methanation (Table 1).

The distinct selectivity for  $CO_2$  hydrogenation of oxides with different phases can be explained by the arrangement of O atoms in the lattice, and the activation of CO<sub>2</sub> and H<sub>2</sub> is affected

simultaneously. Rearrangement of O atoms benefits H<sub>2</sub> dissociation to form O vacancies, which accelerate CO<sub>2</sub> adsorption and transformation. However, the unstable oxide surface can form excessive O vacancies, which might lead to low-coordinated metal atoms for  $CO_2$  methanation.

### 2.2 SMSI on oxides

SMSI was firstly reported by Tauster and Fung<sup>77,78</sup> in the 1970s to study the suppressed CO and H<sub>2</sub> adsorption on the supported metals.<sup>79–84</sup> In these cases, the geometric and electronic modulation of the metal nanoparticles by the oxides plays an important role in optimizing the  $CO_2$  hydrogenation.<sup>12–15,85–88</sup>

TiO<sub>2</sub>- and CeO<sub>2</sub>-supported Rh, Ru and Ir catalysts with high loadings can selectively catalyze  $CO_2$  methanation. With lower metal loadings to reduce the nanoparticle size, these catalysts yield CO as the predominant product. These results are reasonably attributed to the chemical features of the small nanoparticles. Li *et al.*<sup>14</sup> reported the SMSI on an Ir/CeO<sub>2</sub> catalyst, where the partially oxidized Ir nanoparticles exhibit relatively weak CO adsorption, resulting in rapid CO desorption rather than hydrogenation to CH<sub>4</sub> (Fig. 3a–d).<sup>89</sup> Similarly, the atomically dispersed RuO<sub>x</sub> species, which might be generated during the oxidative treatment, could maintain the oxidized state even under the reaction conditions with a reductive atmosphere, because of the strong bonding with the CeO<sub>2</sub> support.<sup>15</sup>

DFT calculations provide mechanistic understanding of the SMSI-controlled product selectivity. Fig. 3e shows the difference between CO dissociation barriers and CO desorption free energies of single-atom Ir (Ir<sub>1</sub>) and stepped Ir (Ir<sub>3</sub>).<sup>88</sup> The stepped Ir shows a much lower value than that of the single atom Ir, suggesting preferentially occurring CO desorption on the single-atom Ir, which could explain the highly selective RWGS reaction. In addition, the difference between C–O dissociation to  $^*CH$  and dehydrogenation of  $^*CHO$  to  $^*CO$  on the single-atom Ir is greatly increased compared to that of the stepped



Table 1 Representative catalysts for tuning the selectivity of CO<sub>2</sub> hydrogenation and their performances

Catalyst	H <sub>2</sub> : CO <sub>2</sub> ratio	Temperature (°C)	Pressure (MPa)	CO <sub>2</sub> conversion (%)	Selectivity (%)		Rate (mmol g <sub>cat</sub> <sup>-1</sup> h <sup>-1</sup> )	
					CO	CH <sub>4</sub>	CO	CH <sub>4</sub>
Rh/TiO <sub>2</sub> (ref. 13)	1 : 1	200	0.1	0.4	92.3	7.7	0.48	0.04
Ir/CeO <sub>2</sub> (ref. 14)	4 : 1	300	1.0	6.8	100	0	6.9	0
Ru/CeO <sub>2</sub> (ref. 15)	4 : 1	240	0.1	<5	92.1	7.9	21.0	1.8
PtCo/TiO <sub>2</sub> (ref. 16)	2 : 1	300	0.1	8.2	98.8	1.2	43.4	0.5
PtCo/CeO <sub>2</sub> (ref. 16)	2 : 1	300	0.1	9.1	92.3	7.7	40.5	3.4
PtCo/ZrO <sub>2</sub> (ref. 16)	2 : 1	300	0.1	7.8	89.5	10.5	39.3	4.6
Co <sub>3</sub> O <sub>4</sub> (ref. 17)	3 : 1	350	0.1	10.0	95.0	5.0	38.1	2.0
Mo <sub>2</sub> C <sup>18</sup>	2 : 1	300	0.1	8.7	93.5	6.5	43.6	3.0
Co/Mo <sub>2</sub> C <sup>18</sup>	2 : 1	300	0.1	9.5	98.1	1.9	49.9	1.0
Rh@S-1 (ref. 19)	3 : 1	500	1.0	51.6	79.8	20.2	13.2	3.4
Ni-in-Cu <sup>20</sup>	3 : 1	550	0.1	50.7	100	0	181.1	0
Ni-Au <sup>21</sup>	3 : 1	600	0.1	18.0	95.0	5.0	109.9	5.8
Rh/NbOPO <sub>4</sub> (ref. 22)	3 : 1	500	2.0	39.9	98.9	1.1	58.1	0.6
Co/r-TiO <sub>2</sub> (ref. 69)	4 : 1	400	3.0	85.0	1.0	99.0	0.5	54.1
Co/a-TiO <sub>2</sub> (ref. 69)	4 : 1	400	3.0	15.0	90.0	10.0	8.7	1.0
Ru/r-TiO <sub>2</sub> (ref. 85)	4 : 1	400	0.1	57.0	3.0	97.0	0.05	1.6
Ru/a-TiO <sub>2</sub> (ref. 85)	4 : 1	400	0.1	23.0	100	0	0.66	0
Ni <sub>3</sub> Fe <sub>9</sub> /ZrO <sub>2</sub> (ref. 101)	2 : 1	400	0.1	18.6	95.8	3.7	22.1	0.9
Cu/β-Mo <sub>2</sub> C <sup>109</sup>	2 : 1	600	0.1	40.0	99.2	0.8	1771.4	14.3
InNi <sub>3</sub> C <sub>0.5</sub> (ref. 111)	3 : 1	500	0.1	53.0	97.0	3.0	117.6	3.6
Ni/SiO <sub>2</sub> (ref. 112)	4 : 1	750	0.1	58.0	100	0	2071.4	0

Ir. C–O bond cleavage of the main intermediates (\*HCOO, \*COOH, and M–CO) strongly determines the CO<sub>2</sub> hydrogenation selectivity.

In addition, \*H spillover also plays a significant role in this reaction.<sup>85</sup> For example, Ru/a-TiO<sub>2</sub> and Ru/r-TiO<sub>2</sub> could selectively catalyze RWGS and methanation, respectively. In addition to the influence of the crystalline phase on \*CO adsorption in the aforementioned discussion, it is found that the hydrogen spillover is important for the reaction. The H atoms from H<sub>2</sub> dissociation at metallic sites could spill to the TiO<sub>2</sub> surface and form Ti–O(H)–Ti species, leading to electron donation into shallow trap states in the band gap of TiO<sub>2</sub>.<sup>90,91</sup> Identified by the band at 1740 cm<sup>-1</sup> in diffuse reflectance infrared Fourier transform spectroscopy (DRIFTS), \*H spillover is more likely to occur on the Ru/a-TiO<sub>2</sub> compared with Ru/r-TiO<sub>2</sub>. That leads to charge transfer from Ru to a-TiO<sub>2</sub>, reducing the π back-donation from Ru to adsorbed \*CO, which results in quick desorption of \*CO and hinders deep hydrogenation to methane.

Besides the classical SMSI, a new type of SMSI was developed by Matsubu *et al.*,<sup>13</sup> which is realized by pretreating the Rh/TiO<sub>2</sub> catalyst in mixed gases of CO<sub>2</sub> and H<sub>2</sub> with a ratio of 10 : 1 to form carbonate-containing species in the overlayer (Fig. 3f and g). It is denoted as adsorbate-induced SMSI (A-SMSI). The amorphous overlayer on the Rh nanoparticles contains a mixture of Ti species (Ti<sup>4+</sup>/Ti<sup>3+</sup> at 7/3), different from the classical SMSI overlayer on the TiO<sub>2</sub> support by H<sub>2</sub> treatment, where the Ti species are dominantly in the Ti<sup>3+</sup> state.<sup>92,93</sup> It is proposed that the adsorbed HCO<sub>x</sub> species might coordinate with TiO<sub>x</sub> in the overlayer, and change the surface properties of the Rh nanoparticles. The redshift and decreased intensity of the linear CO in DRIFTS indicate the weakened CO adsorption,

because of the physically blocked Rh nanoparticles and the polarization of CO bonds induced by charge transfer to Rh. In the CO<sub>2</sub> hydrogenation, the Rh/TiO<sub>2</sub> catalyst with A-SMSI shows 90% selectivity for CO formation, which is different from the general Rh catalysts with dominant CO<sub>2</sub> methanation (Fig. 3h and i).

As observed in these examples, the adjustments of crystal phases of oxides and construction of SMSI on supported catalysts are efficient routes for hindering the CO<sub>2</sub> deep hydrogenation. The features of SMSI, including weakening \*CO adsorption, inhibiting C–O dissociation and deep hydrogenation, and optimizing \*H spillover, are emphasized.

These examples for SMSI show great success on the selectivity control in CO<sub>2</sub> hydrogenation over oxide-supported catalysts. However, the formation of the SMSI still relies on the reducible oxides. In addition, high CO selectivity is always obtained at low conversion of CO<sub>2</sub> (<5%). Also, the classical SMSI could be destroyed by re-oxidation from water or oxygen at high temperature.<sup>12–15</sup> To overcome this limitation, exploiting new supports or catalysts for this reaction is always important.

### 3. Phosphate-based catalysts

SMSI has been reported on phosphates such as hydroxyapatite (HAP) and LaPO<sub>4</sub> for CO oxidation.<sup>94–96</sup> It also plays a role in tuning the selectivity of CO<sub>2</sub> hydrogenation. Wang *et al.*<sup>22</sup> reported a Rh/NbOPO<sub>4</sub> catalyst with phosphate-based SMSI for highly active and selective RWGS reaction, which is quite different from the general Rh catalyst in CO<sub>2</sub> methanation. The Rh nanoparticles with small size at 1.1 nm are uniformly dispersed on the NbOPO<sub>4</sub> support, exhibiting CO as



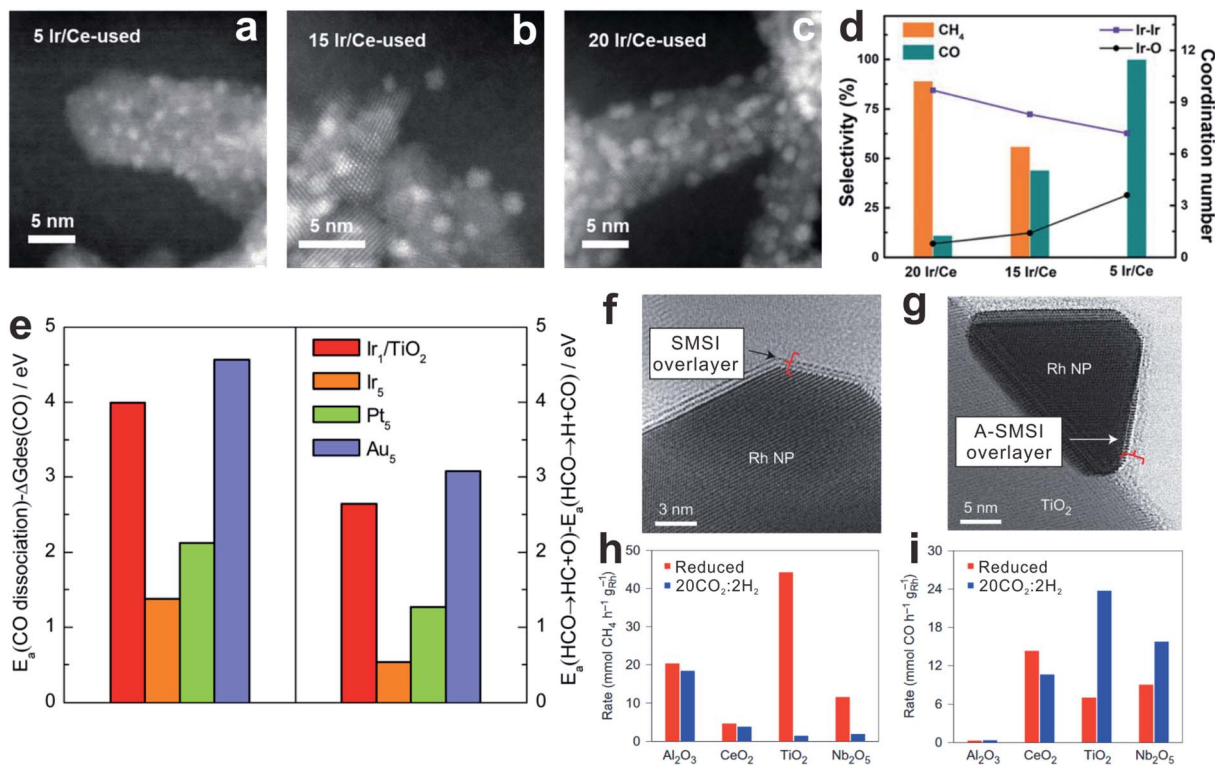


**Fig. 3** (a–c) HAADF-STEM images of catalysts: (a) 5 Ir/Ce used, (b) 15 Ir/Ce used, and (c) 20 Ir/Ce used. (d) The coordination number of Ir–Ir and Ir–O shells (data, right axis) relative to catalytic selectivity (bars, left axis) of Ir/Ce catalysts with different Ir loadings. Reproduced with permission from ref. 14. Copyright (2017) Wiley-VCH. (e) Left: difference between activation energies for CO dissociation and desorption free energies of CO. Right: difference in activation energies between  $\text{HCO} \rightarrow \text{HC} + \text{O}$  and  $\text{HCO} \rightarrow \text{H} + \text{CO}$  on  $\text{Ir}_1/\text{TiO}_2$ , and stepped Ir ( $\text{Ir}_5$ ), Pt ( $\text{Pt}_5$ ), and Au ( $\text{Au}_5$ ) surfaces. Reproduced with permission from ref. 88. Copyright (2017) American Chemical Society. (f and g) *In situ* STEM images of (f) an SMSI overlayer, a  $\text{TiO}_x$  crystalline bilayer containing exclusively  $\text{Ti}^{3+}$ , and (g) an A-SMSI overlayer, an amorphous  $\text{TiO}_x$  overlayer containing a mixture of  $\text{Ti}^{3+}$  and  $\text{Ti}^{4+}$ , on the surface of Rh nanoparticles. (h)  $\text{CH}_4$  and (i) CO generation rates on 2% Rh with various supports after reduction or  $20\text{CO}_2 : 2\text{H}_2$  treatment. Reproduced with permission from ref. 13. Copyright (2017) Springer Nature.

a predominant product in  $\text{CO}_2$  hydrogenation in a wide temperature range of 200–500 °C (Fig. 4a). The catalyst with Rh loading at 0.7% gives  $\text{CO}_2$  conversion of 39.9% with CO selectivity of 98.9%. Such performance remarkably outperforms the Rh nanoparticles on  $\text{CeO}_2$ ,  $\text{TiO}_2$ , and  $\text{Nb}_2\text{O}_5$  supports with SMSI.

The SMSI between Rh and a  $\text{NbOPO}_4$  support is explored by  $\text{H}_2$ -TPR and CO-TPD tests, where the reduction temperatures of  $\text{Rh}^+ \rightarrow \text{Rh}^0$  are increased and the desorption temperatures of

CO are decreased, compared with the generally supported Rh catalysts. In addition, the Rh/ $\text{NbOPO}_4$  sample gives the lowest  $\text{Rh}^0/\text{Rh}^{3+}$  ratio among these catalysts identified by XPS, due to the electronic interactions on the Rh– $\text{NbOPO}_4$  interface to stabilize the positively charged Rh.<sup>82</sup> The Rh/ $\text{NbOPO}_4$  catalyst also exhibits decreased CO adsorption, where only the weak stretches of *gem*-dicarbonyl  $\text{Rh}(\text{CO})_2$  species<sup>12,13,97,98</sup> are observed in CO-adsorption DRIFTS (Fig. 4b). In the  $\text{CO}_2$

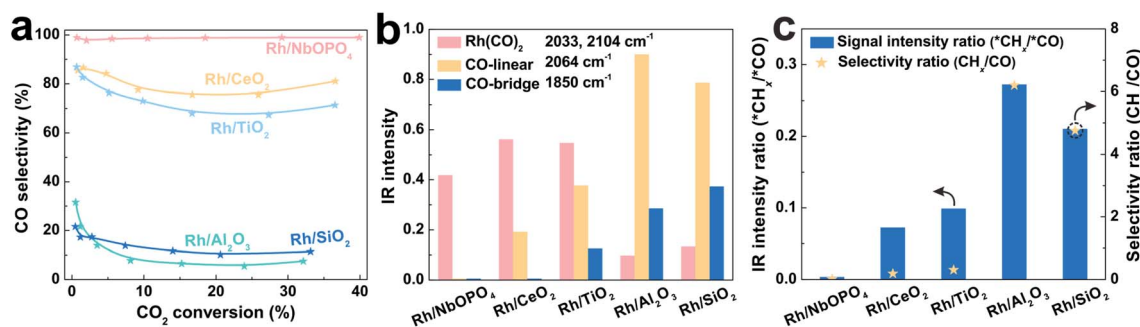


**Fig. 4** (a) Dependence of CO selectivity on  $\text{CO}_2$  conversion (a) over various catalysts at 200–500 °C. (b) DRIFTS peak intensities characterizing the different CO species adsorbed on various catalysts. (c) Correlation of DRIFTS peak intensity and selectivity in  $\text{CO}_2$  hydrogenation over various catalysts. Reproduced with permission from ref. 22. Copyright (2020) Wiley-VCH.



hydrogenation (Fig. 4c), *in situ* DRIFTS shows that the  $^*CH_x$  species, a crucial intermediate for  $CH_4$  formation, can be observed on the other catalysts, but is undetectable on the Rh/NbOPO<sub>4</sub> catalyst, in agreement with the highly selective RWGS.

Therefore, the high CO selectivity for the Rh/NbOPO<sub>4</sub> catalyst in CO<sub>2</sub> hydrogenation could be explained by the decreased  $^*CO$  adsorption, resulting from the SMSI between Rh and NbOPO<sub>4</sub>, which is similar to the phenomena on the general oxide-supported catalysts with SMSI. Although it is observed that phosphate-based SMSI tunes the Rh catalyst from CO<sub>2</sub> methanation to RWGS, the influence on CO<sub>2</sub> hydrogenation still needs further *operando* characterization and theoretical investigations. This observation still provides a new type of catalyst for CO<sub>2</sub> hydrogenation with optimized selectivity.

## 4. Alloy-based catalysts

Inspired by the catalysts with SMSI for weak adsorption of the  $^*CO$  intermediate to selectively obtain the CO product in CO<sub>2</sub> hydrogenation, it is reasonable that construction of alloyed metal catalysts with variable adsorption of the  $^*CO$  intermediate could be adjusted by the alloyed compositions and supports.<sup>99,100</sup> Recently, alloys of PtCo, NiFe, CuNi and NiAu<sup>16,20,21,101,102</sup> have been reported for tuning product selectivity in CO<sub>2</sub> hydrogenation.

Kattel *et al.*<sup>16</sup> reported CO<sub>2</sub> hydrogenation over PtCo bimetallic catalysts supported on oxides of CeO<sub>2</sub>, ZrO<sub>2</sub>, and TiO<sub>2</sub>, which all give RWGS as a dominant reaction. Particularly, PtCo/TiO<sub>2</sub> gives a much higher CO/CH<sub>4</sub> ratio than those of PtCo/CeO<sub>2</sub> and PtCo/ZrO<sub>2</sub>. On the PtCo/TiO<sub>2</sub> catalyst, the energy barrier of  $^*CO$  desorption is much lower than that for hydrogenation to  $^*CHO$ , leading to the generation of gas phase CO (Fig. 5a and b). In contrast, energy for  $^*CO$  hydrogenation is comparable with that of  $^*CO$  desorption on the PtCo/ZrO<sub>2</sub> catalyst, resulting in the formation of CH<sub>4</sub> or CH<sub>3</sub>OH as competitive reactions, evidenced by DRIFTS and ambient-pressure X-ray photoelectron spectroscopy (AP-XPS).

These PtCo catalysts provide an example for tuning the product selectivity in CO<sub>2</sub> hydrogenation, which combines the advantages of alloys and oxide supports. Investigations on ZrO<sub>2</sub>-supported NiFe catalysts reveal the structure–performance relationship of catalyst interfaces.<sup>101</sup> Ni<sub>3</sub>/ZrO<sub>2</sub> is highly active for CO<sub>2</sub> methanation (CO<sub>2</sub> conversion of 34.2% and CH<sub>4</sub> selectivity of 84.7%), while Fe<sub>3</sub>/ZrO<sub>2</sub> shows low activity, but is highly selective for CO production (CO<sub>2</sub> conversion of 3.1% and CO selectivity of 100%). Interestingly, upon introducing Ni to an Fe-based catalyst, the activity is markedly increased, and the CO selectivity can be tuned from 11.5% to 91.8% by adjusting the Ni/Fe ratios. Generally, the Ni–ZrO<sub>2</sub> interface is regarded as the active site for CO<sub>2</sub> methanation. However, when a large amount of Fe species is introduced, the dispersed Fe species would cover the Ni particles to form Ni–FeO<sub>x</sub> interfaces, which changes the product selectivity in the CO<sub>2</sub> hydrogenation. Therefore, CO<sub>2</sub> methanation occurs on the Ni/ZrO<sub>2</sub> catalyst *via* the RWGS + CO hydrogenation pathway, but fails on the NiFe/ZrO<sub>2</sub> catalyst which gives CO as the predominant product.

Because of the structural nonuniformity of the catalysts, it is still difficult to investigate the relationship between the catalyst structure and catalytic performance. Moreover, addition of promoters/additives might result in the formation of new active sites and interfaces for CO<sub>2</sub> adsorption and transformation. Wang *et al.*<sup>20</sup> reported a CuNi alloy-based catalyst (Ni-in-Cu), showing highly dispersed Ni incorporated into the Cu lattice, which combines the advantages of high activity of Ni and high selectivity of Cu. The Ni-in-Cu catalyst gives a CO<sub>2</sub> conversion of 1.1–50.7%, and the CO selectivity always remains at 100%. The superior CO selectivity is obtained even under conditions with H<sub>2</sub>/CO<sub>2</sub> ratios in a wide range of 1–9 (Fig. 5c). In comparison, the general Cu (ref-Cu) and Ni (ref-Ni) catalysts show much lower CO<sub>2</sub> conversion and CO selectivity than those of the Ni-in-Cu catalyst. In these cases, the atomic dispersion of Ni in the Cu lattice is crucial for such performance, and the ref-CuNi catalyst with the same composition but partially separated Cu and Ni phases yields the methane product under equivalent reaction conditions.

More importantly, the simple and uniform structure of the Ni-in-Cu catalyst provides a model for mechanistic investigation to identify the reaction routes and active sites. By *in situ* DRIFTS and XPS studies, the CO<sub>3</sub><sup>2-</sup>, CO<sub>2</sub><sup>δ-</sup> and HCO<sub>3</sub><sup>-</sup> species are observed on the catalyst surface, giving decreased signals during the CO<sub>2</sub> hydrogenation, which indicate their important roles as the intermediates for CO formation. In contrast,  $^*HCOO$  is formed and remains unchanged during this process, which is attributed to the fact that this species is stable and difficult to be hydrogenated.<sup>33</sup> Combining various characterization techniques, it has been found that the CO<sub>2</sub> molecules simultaneously interact with Cu and Ni sites on the surface of the CuNi alloy. When CO is formed from the C=O cleavage of CO<sub>2</sub>, it rapidly desorbs from the catalyst surface to avoid deep hydrogenation (Fig. 5d). DFT calculations reveal the easy C=O cleavage of CO<sub>2</sub> to form CO on the CuNi(111) surface. Because CO can easily desorb from the catalytic surface, it is difficult to form  $^*HCO$  by hydrogenation (Fig. 5e), which is due to the fact that H atoms preferentially remove the isolated O atoms on the CuNi(111) surface *via* an exothermic process with energy barriers of –0.31/–0.75 eV. In contrast,  $^*CO$  hydrogenation to  $^*HCO$  is an endothermic step with energy barriers of 1.40/0.78 eV. These results demonstrate the multifunctionality of CuNi alloy sites on the Ni-in-Cu catalyst, which embodies the efficient CO<sub>2</sub> activation and H<sub>2</sub> dissociation, and accelerates the CO desorption, benefiting the RWGS reaction but switching off the methanation.

Zhang *et al.*<sup>21</sup> reported a Ni–Au bimetallic catalyst with a core–shell structure, where the Au shell is always in contact with the Ni core. The core–shell structure kinetically transforms to a NiAu alloy during the CO<sub>2</sub> hydrogenation, and reverses after the reaction. In this process, CO is a dominant product with selectivity higher than 95%. In the environmental transmission electron microscopy (ETEM) characterization (Fig. 6a) at near-ambient pressure (9 ± 0.1 mbar, 25% CO<sub>2</sub>/75% H<sub>2</sub>), the ultra-thin Au shell is observed around the Ni@Au nanoparticles at 400–500 °C, and disappears to form a NiAu alloy at 600 °C. The segregation energy ( $E_{seg}$ ) of the Ni atom from the bulk to the



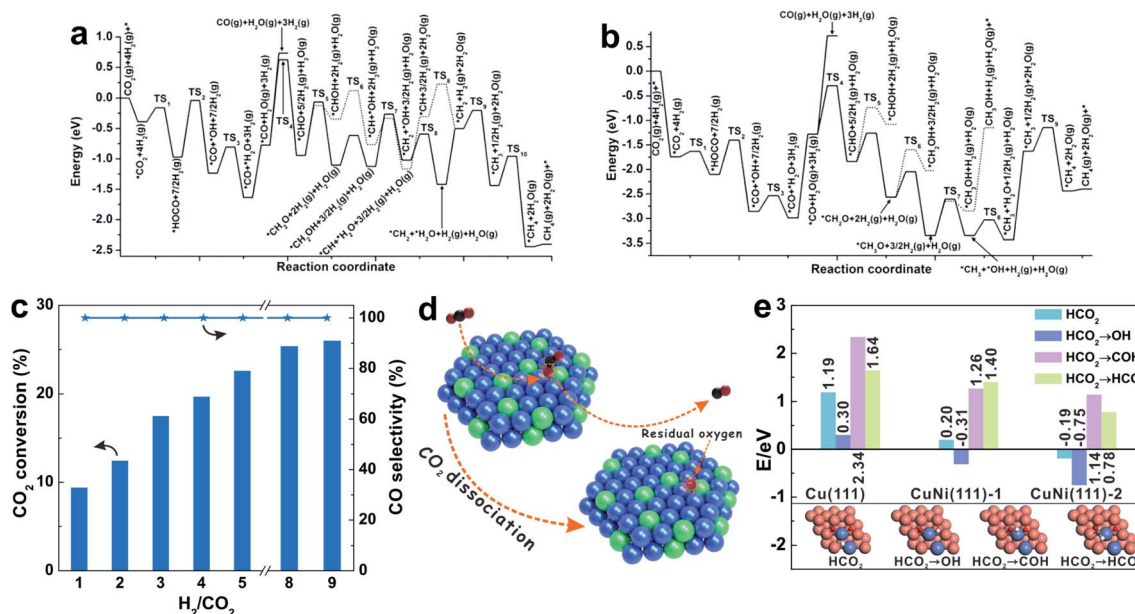


Fig. 5 (a and b) Potential energy diagrams for the synthesis of CO and CH<sub>4</sub> through the RWGS and CO hydrogenation pathway, on the hydroxylated (a) Ti<sub>3</sub>O<sub>6</sub>/PtCo(111) and (b) Zr<sub>3</sub>O<sub>6</sub>/PtCo(111) surfaces. Reproduced with permission from ref. 16. Copyright (2016) Wiley-VCH. (c) Dependence of CO<sub>2</sub> conversion and CO selectivity on the feed H<sub>2</sub>/CO<sub>2</sub> ratio with the Ni-in-Cu catalyst at 673 K. Various H<sub>2</sub>/CO<sub>2</sub> ratios balanced with 10% Ar in the feed gas. (d) Schematic illustration of the CO<sub>2</sub> dissociation on the Ni-in-Cu catalyst. (e) Enthalpies of the reaction of H migration on various surfaces: H adsorbed on catalyst surfaces (HCO<sub>2</sub>), H adsorbed on oxygen atoms (HCO<sub>2</sub> → OH), H adsorbed on the oxygen of CO (HCO<sub>2</sub> → COH), and H adsorbed on the carbon of CO (HCO<sub>2</sub> → HCO). Reproduced with permission from ref. 20. Copyright (2020) American Chemical Society.

surface Au layer was calculated. The  $E_{\text{seg}}$  can be reduced by the adsorbed species, such as H<sub>2</sub>, \*H, \*OH and \*CO, on the Au surface (Fig. 6b). Particularly, the minimized  $E_{\text{seg}}$  is obtained under CO adsorption, which helps Ni transfer to the Au layer to form a NiAu alloy. These results are also in agreement with the fact that the NiAu alloy is detected during the CO<sub>2</sub> hydrogenation, but disappears after the reaction. Moreover, the CO<sub>2</sub> hydrogenation on the NiAu alloy undergoes a two-step pathway. In the first step, CO<sub>2</sub> hydrogenation to CO occurs on Ni sites with an energy barrier of 0.89 eV. In the second step, CO prefers to diffuse from Ni to Au sites and desorbs, with energy barriers of 1.23 and 0.45 eV, respectively. In contrast, both dissociation and deep hydrogenation of CO need to overcome higher energy barriers. Therefore, it is a virtuous circle that the NiAu alloy is a selective catalytic surface for the RWGS reaction. Notably, CO could benefit the formation of the NiAu alloy, which is evidenced by NiAu alloy formation after quenching in CO rather than H<sub>2</sub> or N<sub>2</sub> (Fig. 6c).

The metal alloy based-catalysts play a role in decreasing the energy barriers of the \*CO desorption, to a level below \*CO dissociation or deep hydrogenation. Compared to the SMSI that also has similar functions in weakening CO adsorption, the alloyed interfaces exhibit more adjustable properties, because of their precisely controllable metal compositions and electronic structures. These observations on the alloy based-catalysts convincingly demonstrate that an appropriate binding strength of intermediates, throughout the CO<sub>2</sub> hydrogenation, is a key to controlling product selectivity.

## 5. Carbide-based catalysts

Transition metal carbides (TMCs) are well known to have excellent catalytic properties, which are similar to those of noble metal catalysts. The high activity of carbides originates from the carbon, and results in modulating the electronic properties, and tuning the binding energies of reaction intermediates.<sup>103,104</sup> Metal carbides have been extensively used in reforming<sup>105,106</sup> and WGS<sup>107,108</sup> reactions. Also, they are promising for CO<sub>2</sub> hydrogenation because of the dual functions of H<sub>2</sub> dissociation and C=O bond scission.<sup>109–112</sup>

Porosoff *et al.*<sup>18</sup> reported CO<sub>2</sub> hydrogenation on defined Mo<sub>2</sub>C surfaces, which are highly active and selective for CO production. The Mo<sub>2</sub>C catalyst shows a CO<sub>2</sub> conversion of 8.7% and CO/CH<sub>4</sub> ratio of 14.5 for CO<sub>2</sub> hydrogenation at 300 °C, outperforming noble metal bimetallic catalysts. The catalytic performance can be further improved by modification with Co, a well-known catalyst for methanation or Fischer–Tropsch synthesis to produce alkanes. CO<sub>2</sub> conversion and CO selectivity of 9.5% and 51.3% (CO/CH<sub>4</sub> product ratio of 51.3) were obtained on the Co–Mo<sub>2</sub>C catalyst. By employing temperature-programmed surface reaction (TPSR), the Mo<sub>2</sub>C surface is proved to be the active phase. In AP-XPS experiments (Fig. 7), when CO<sub>2</sub> gas is introduced into the Mo<sub>2</sub>C catalyst, a signal assigned to O–Mo–C at 283.6 eV appears,<sup>113</sup> rather than CO<sub>3</sub><sup>2-</sup>, CO<sub>2</sub><sup>δ-</sup> and \*HCOO species, suggesting a different pathway for CO<sub>2</sub> activation on the Mo<sub>2</sub>C. It is proposed that CO<sub>2</sub> directly reacts with Mo<sub>2</sub>C through the lone-pair electrons on the O atom to produce CO and an oxycarbide surface (Mo<sub>2</sub>C–O), which is



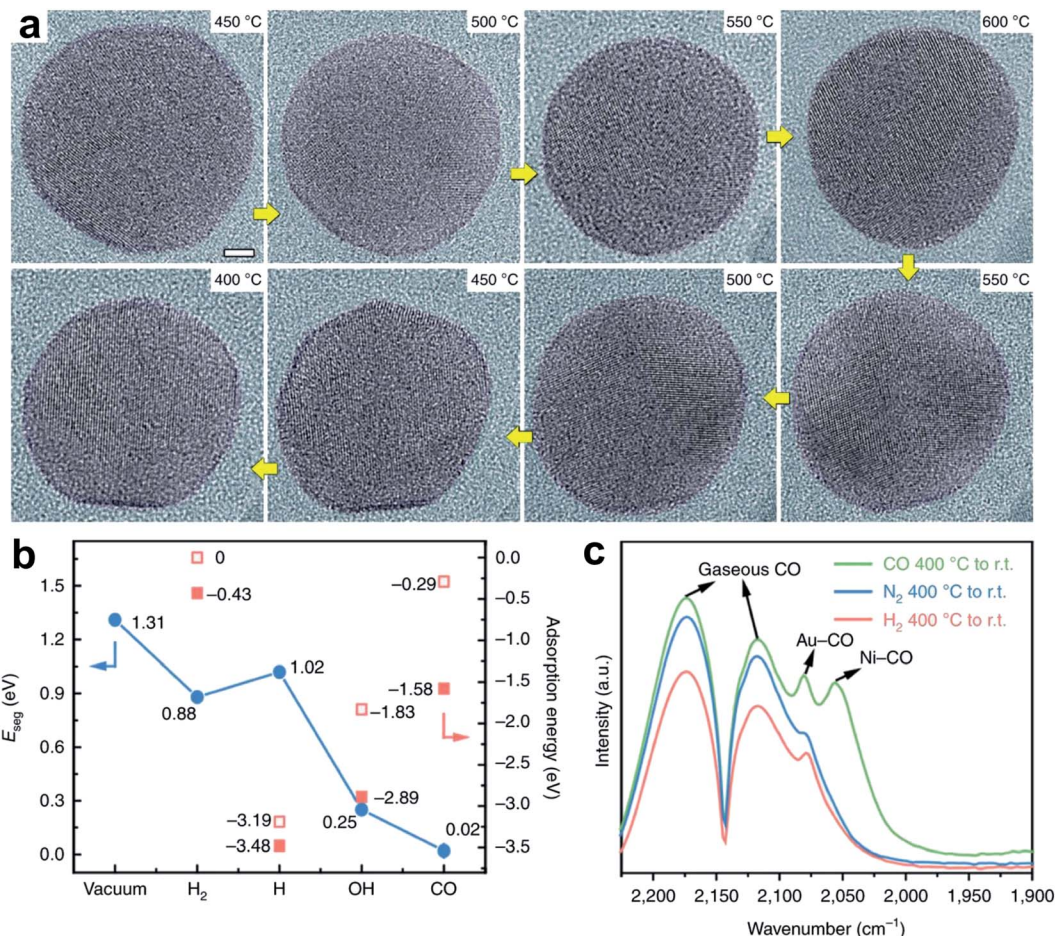


**Fig. 6** (a) *In situ* TEM images of the alloying and dealloying evolution of an individual NiAu particle during the CO<sub>2</sub> hydrogenation reaction. Scale bar, 2 nm. (b) Segregation energy ( $E_{\text{seg}}$ ) of the adsorption of H<sub>2</sub>, H, OH and CO under vacuum (blue dots), and the adsorption energies of different adsorbates when all the Ni atoms are located in the bulk (hollow pink squares) and when a single Ni atom is moved to the Au surface (solid pink squares). (c) FTIR spectra using CO as the probing molecule after fast quenching in H<sub>2</sub>, N<sub>2</sub> and CO. Reproduced with permission from ref. 21. Copyright (2020) Springer Nature.

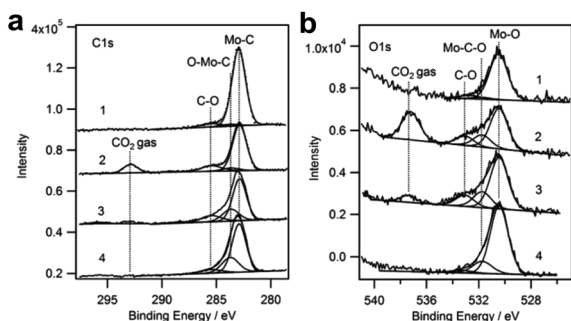


**Fig. 7** AP-XPS of (a) C 1s and (b) O 1s of Mo<sub>2</sub>C under various treatment conditions for CO<sub>2</sub> activation. (1) Clean Mo<sub>2</sub>C; (2) 150 mTorr CO<sub>2</sub> at room temperature; (3) 150 mTorr CO<sub>2</sub> + 550 mTorr H<sub>2</sub> with annealing to 523 K, followed by cooling to room temperature; (4) 150 mTorr CO<sub>2</sub> + 550 mTorr H<sub>2</sub> at 523 K. Reproduced with permission from ref. 18. Copyright (2014) Wiley-VCH.

subsequently reduced by H<sub>2</sub> to regain the Mo<sub>2</sub>C surface. Notably, the unreduced MoO<sub>x</sub> species always exists in the Mo<sub>2</sub>C catalyst, with a ratio of 16.8% identified by *in situ* X-ray

absorption near edge spectroscopy (XANES). Introducing Co into the Mo<sub>2</sub>C catalyst leads to the formation of a new CoMoC<sub>3</sub>O<sub>2</sub> phase during the reduction process. The CoMoC<sub>3</sub>O<sub>2</sub> phase is highly active for CH<sub>4</sub> dissociation,<sup>114</sup> which further increases the CO selectivity, in agreement with the much higher CO/CH<sub>4</sub> ratio obtained on the Co-Mo<sub>2</sub>C catalyst.

Because of the excellent properties, Mo<sub>2</sub>C was further coupled with other metals, such as Cu, a classical catalyst for CO<sub>2</sub> hydrogenation. Zhang *et al.*<sup>109</sup> reported a Cu/β-Mo<sub>2</sub>C catalyst, which shows extraordinary RWGS activity, selectivity, and stability. The Cu/β-Mo<sub>2</sub>C exhibits acceptable deactivation after six-cycle start-up-cool-down tests, and maintains 85% of its initial activity after 40 h reaction at a high reaction temperature of 600 °C. Cu<sup>+</sup> species are detected on the Cu/β-Mo<sub>2</sub>C catalyst, suggesting a strong interaction between Cu and Mo<sub>2</sub>C. Such interaction helps in Cu nanoparticle stabilization, modulates the electronic structure for efficient CO<sub>2</sub> activation and hinders Cu sintering. In the CO<sub>2</sub> dissociation experiments without H<sub>2</sub>, the Cu/β-Mo<sub>2</sub>C catalyst exhibits much higher CO production than that of β-Mo<sub>2</sub>C





and Cu/ZnO/Al<sub>2</sub>O<sub>3</sub>. These results support the mechanism of the RWGS reaction on Mo<sub>2</sub>C catalysts involving two steps, CO<sub>2</sub> dissociation on the catalytic surface and H<sub>2</sub> reduction of the residual O species.<sup>18,115</sup>

Moreover, Zhang *et al.*<sup>110</sup> coupled the high activity of Mo<sub>2</sub>C and the non-thermal plasma (NTP) technique to produce CO. The TOF activity of β-Mo<sub>2</sub>C nanorods in NTP-catalysis (applying NTP and the catalyst, without heating) is two orders of magnitude higher than that obtained under catalysis-only conditions (applying the catalyst and heating) (Fig. 8a and b), for example, 26.0 s<sup>-1</sup> and 0.55 s<sup>-1</sup> for NTP catalysis and thermal catalysis-only conditions, respectively. In the designed reaction between CO<sub>2</sub> and the catalyst surface, CO was detected immediately upon introducing a CO<sub>2</sub>/Ar flow. It is suggested that the CO originates from direct CO<sub>2</sub> dissociation, which facilitates the high CO selectivity, in agreement with reports on carbide-based catalysts. In the NTP-catalysis, CO<sub>2</sub> and H<sub>2</sub> can be vibrationally excited and dissociated by plasma. In the first-step CO<sub>2</sub> dissociation test (Fig. 8c–e), β-Mo<sub>2</sub>C nanorods under NTP-only conditions (applying NTP, without catalyst and heating) show

a 20 times higher CO signal than that under catalysis-only conditions, indicating that NTP can promote CO<sub>2</sub> dissociation. In the meanwhile, an abundant O<sub>2</sub> signal is detected, which originates from the three-body (M) recombination of dissociative O atoms from split CO<sub>2</sub>. NTP-catalysis also exhibits a stronger CO signal, in agreement with the high activity and weaker O<sub>2</sub> signal due to the O affinity of carbides,<sup>18</sup> evidenced by abundant H<sub>2</sub>O generated in the second-step H<sub>2</sub> treatment. In addition, NTP can help the decomposition of \*HCOO adsorbed on the catalyst, facilitating the CO production and regaining the catalytic surface.<sup>116</sup> Overall, the NTP-catalysis exhibits a synergistic enhancement for the RWGS reaction. The NTP induces vibration, excitation and dissociation of reactants, which subsequently interact with β-Mo<sub>2</sub>C. In this process, β-Mo<sub>2</sub>C exists as a platform for various intermediates to accelerate the reaction. The highly porous structure of β-Mo<sub>2</sub>C nanorods provides a large accessible surface, modifies the electron energy distribution, and expands the discharge region, which not only promote the formation of charge-induced intermediates, but also change the adsorption and desorption.<sup>117</sup> The molecule-

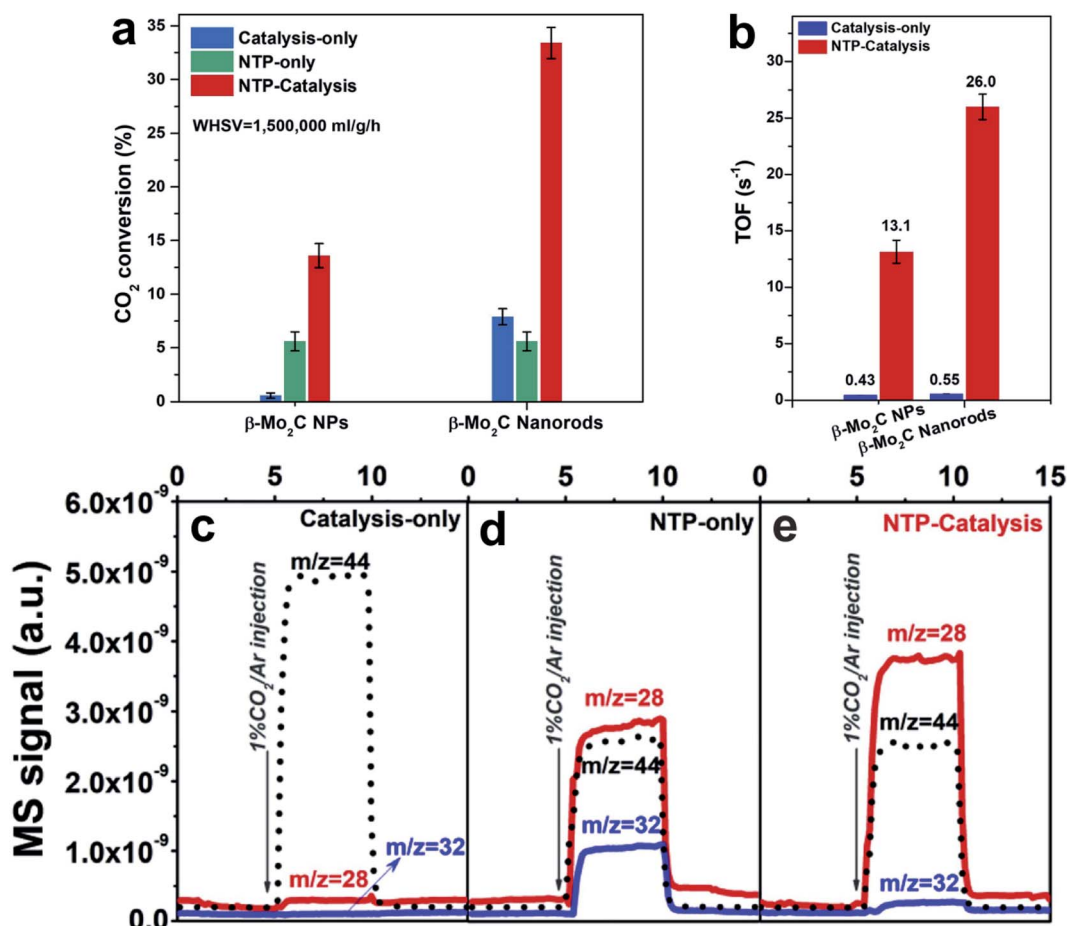


Fig. 8 (a) CO<sub>2</sub> conversion under catalysis-only (at 350 °C), NTP-only, and NTP catalysis conditions (input power of ca. 36 W) over β-Mo<sub>2</sub>C NP and β-Mo<sub>2</sub>C nanorod catalysts (AP, CO<sub>2</sub> : H<sub>2</sub> = 1 : 2, WHSV = 1 500 000 mL g<sup>-1</sup> h<sup>-1</sup>). (b) TOF comparison over β-Mo<sub>2</sub>C NP and β-Mo<sub>2</sub>C nanorod catalysts under catalysis-only (at 350 °C) and NTP-catalysis conditions (input power of ca. 36 W). (c–e) Surface reaction experiment with injection of 1% CO<sub>2</sub>/Ar under (c) catalysis-only, (d) NTP-only and (e) NTP-catalysis conditions. Reproduced with permission from ref. 110. Copyright (2020) Elsevier.



surface interactions on the  $\beta$ - $\text{Mo}_2\text{C}$  lead to not only superior CO selectivity but also high productivity.

In addition to the  $\text{Mo}_2\text{C}$ , other carbides such as  $\text{Ni}_3\text{C}$  and  $\text{InNi}_3\text{C}_{0.5}$  were explored for  $\text{CO}_2$  hydrogenation.<sup>111,112</sup> Although Ni is highly selective for methanation, both  $\text{Ni}_3\text{C}$  and  $\text{InNi}_3\text{C}_{0.5}$  with carbide structures exhibit superior RWGS features. Chen *et al.*<sup>111</sup> reported that  $\text{InNi}_3\text{C}_{0.5}$  supported on  $\text{Al}_2\text{O}_3/\text{Al}$ -fibers shows over 97% CO selectivity in  $\text{CO}_2$  hydrogenation under wide reaction conditions. For example, the  $\text{CO}_2$  conversion is 53% at 540 °C, which is close to the equilibrium value of 54%. The  $\text{InNi}_3\text{C}_{0.5}$  has an anti-perovskite-type structure containing a stable (111) surface with a hexagonal shape. DFT calculations reveal the dual active sites of 3Ni–In (h1) and 3Ni–C (h2), which give a richer electron density distribution, facilitating activated  $^*\text{H}$  formation and  $\text{CO}_2$  dissociation to CO *via* a redox mechanism.  $\text{CO}_2$  prefers to adsorb on the h1 site, and the dissociated  $^*\text{CO}$  and  $^*\text{O}$  are adsorbed on h2 and h1 sites, respectively. The dissociated  $^*\text{H}$  species are adsorbed on both h1 and h2 sites. The  $^*\text{O}$  on the h1 site could react with  $\text{H}^*$  to form  $^*\text{OH}$ , and two  $^*\text{OH}$  easily convert to  $\text{H}_2\text{O}$ . The dual sites always provide lower energy barriers than those of the sole h1 site, demonstrating the advantages of the dual sites on  $\text{InNi}_3\text{C}_{0.5}$ .

Carbide phases, such as  $\text{Ni}_3\text{C}$ , easily form in Ni catalysts at high reaction temperature, because carbon is highly miscible on the Ni surface.<sup>118</sup> Galhardo *et al.*<sup>112</sup> reported that the  $\text{Ni}_3\text{C}$  phase, which forms in  $\text{CO}_2$  hydrogenation, can switch the

selectivity from  $\text{CH}_4$  to CO. The fresh  $\text{Ni}/\text{SiO}_2$  catalysts show suppressed methanation activity in  $\text{CO}_2$  hydrogenation with CO as a dominant product at a wide temperature range (100–800 °C, Fig. 9a). Catalysts with different Ni loadings, particle sizes, or supports show similar catalytic features of methanation in Run 1, and suppressed selectivity of  $\text{CH}_4$  in Run 2. Under *operando* conditions, energy-dispersive X-ray absorption spectroscopy (ED-XAS) and EXAFS (Fig. 9b and c) reveal that the Ni–C scattering belongs to the  $\text{Ni}_3\text{C}$  structure, which contributes to the selectivity changes. The  $\text{Ni}/\text{SiO}_2$  catalyst exhibits much lower CO-adsorption intensity in DRIFTS after Run 1, suggesting the weak CO-binding ability of the formed  $\text{Ni}_3\text{C}$  surface, which benefits CO desorption. It is further evidenced by DFT calculations that various CO-adsorption modes give higher adsorption energies on the  $\text{Ni}_3\text{C}(001)$  surface, compared to those on the Ni(111) surface (Fig. 9d and e). These results help to explain the suppressed methanation: because  $\text{CO}_2$  adsorption always occurs on the oxide supports, and the activated  $^*\text{H}$  species can spill to reduce  $\text{CO}_2$ , the  $\text{CO}_2$ -to-CO process is not affected by the C atoms covered on Ni. However, the subsequent CO-to- $\text{CH}_4$  process is suppressed, due to the weakened CO adsorption on the  $\text{Ni}_3\text{C}$  phase.

Carbide-based catalysts effectively control the transformation pathways of  $^*\text{CO}$  species. When the  $^*\text{CO}$  adsorption is weakened, the C–O bond cleavage and  $^*\text{CO}$  deep hydrogenation are hindered. The CO formation on the carbides always

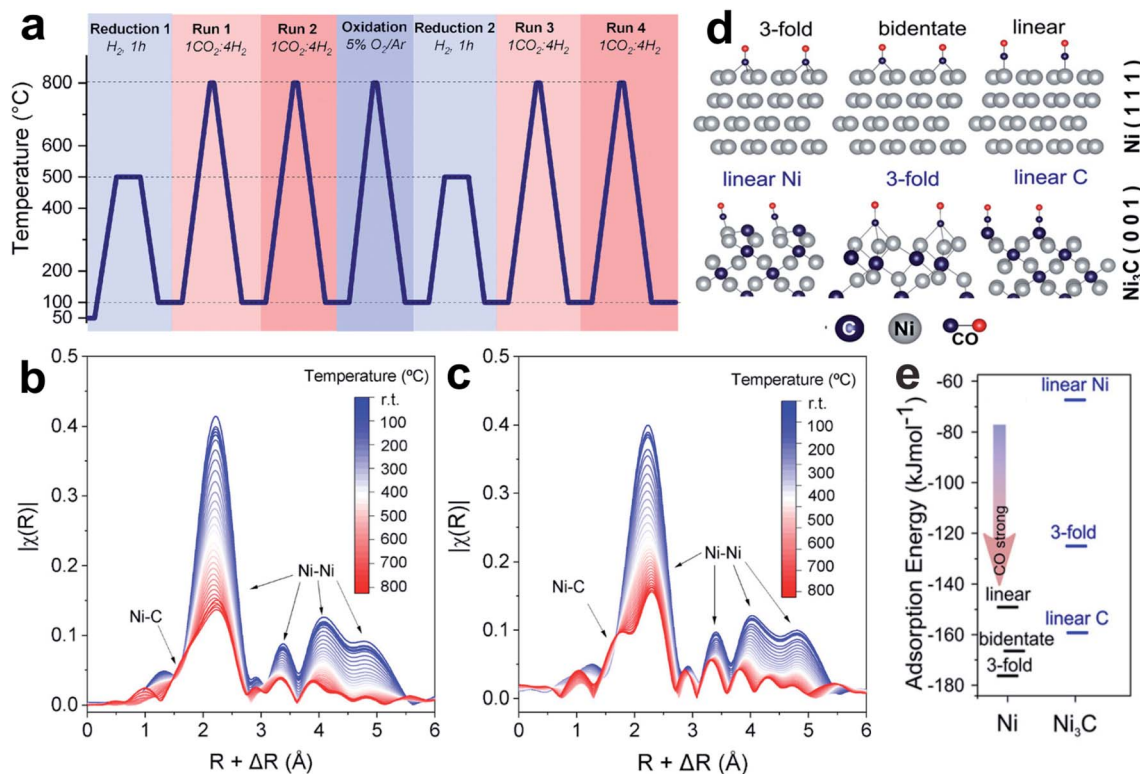


Fig. 9 (a) Experimental setup used to investigate the activity–structure relationships. (b and c) Temperature-resolved Ni K-edge ED-XAS spectra for  $\text{Ni}/\text{SiO}_2$  under  $\text{CO}_2$  hydrogenation conditions during (b) Run 1 and (c) Run 2. (d) CO adsorption structure models at Ni(111) and C-terminated  $\text{Ni}_3\text{C}(001)$ . (e) CO adsorption energy at Ni(111) (dark gray lines) and C-terminated  $\text{Ni}_3\text{C}(001)$  (blue lines). Reproduced with permission from ref. 112. Copyright (2021) American Chemical Society.



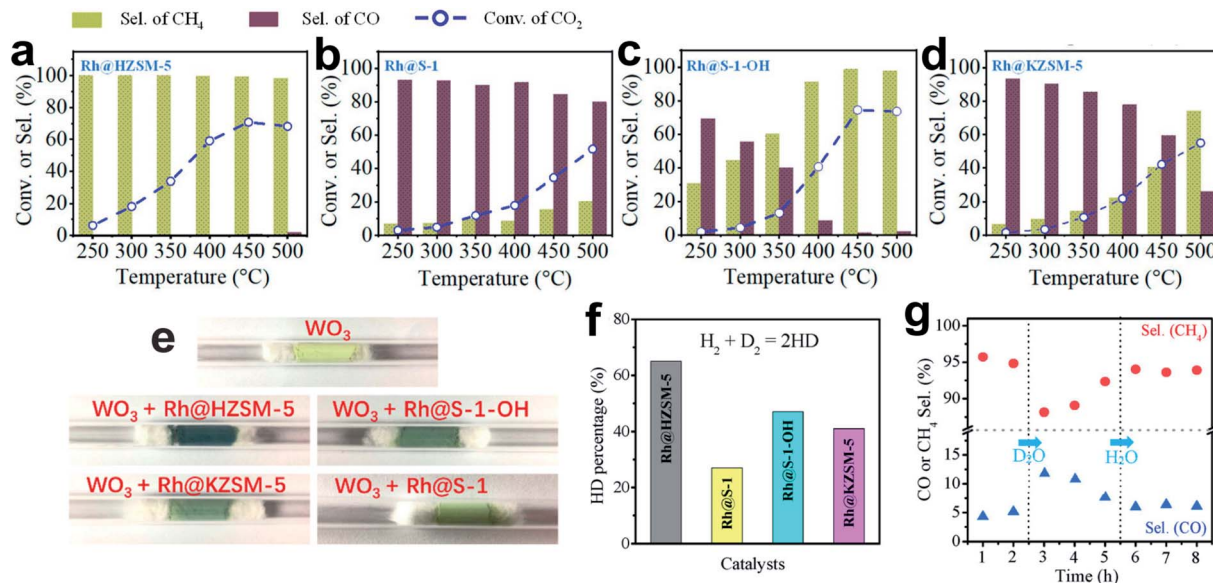


Fig. 10 (a–d) (a) Catalytic performance of (a) Rh@HZSM-5, (b) Rh@S-1, (c) Rh@S-1-OH and (d) Rh@KZSM-5 in CO<sub>2</sub> hydrogenation. Reaction conditions: 0.5 g of catalyst; 1 MPa feed gas pressure, CO<sub>2</sub>/H<sub>2</sub>/Ar = 1/3/1, molar; feed flow rate 30 mL min<sup>-1</sup>. (e) Photographs of samples made with 1 g of WO<sub>3</sub> mixed with 0.02 g of various catalysts after treatment with H<sub>2</sub> at 30 °C for 10 min. (f) Results of H–D exchange experiments with various catalysts. (g) CH<sub>4</sub> and CO selectivity in CO<sub>2</sub> hydrogenation catalyzed by Rh@HZSM-5 treated with D<sub>2</sub>O and H<sub>2</sub>O. Reproduced with permission from ref. 19. Copyright (2019) American Chemical Society.

follows the pathway of direct dissociation of CO<sub>2</sub> to CO *via* a redox mechanism, and because of the strong interaction between the carbide surface and oxygen, an oxycarbide surface could form and subsequently be reduced by H<sub>2</sub>. Sometimes, the unique active phases of carbides even show new functions of catalyzing CH<sub>4</sub> dissociation, further benefiting the selective formation of CO.

## 6. Conclusions and perspectives

In conclusion, the developments for metal-based catalysts to tune product selectivity in CO<sub>2</sub> hydrogenation are briefly summarized. Oxide-supported metal catalysts with classical SMSI show an effective strategy for weakening \*CO and H<sub>2</sub> adsorption to hinder deep hydrogenation. Phosphate-supported metal catalysts with similar phenomena to classical SMSI show even more excellent catalytic performances. Alloy- and carbide-based catalysts exhibit multifunctionality, contributing to reducing the CO desorption energy barrier to a level lower than CO dissociation or deep hydrogenation. Alloy-based catalysts also exhibit satisfactory controllability of the structure–performance relationship by easily adjusting the metal compositions. Carbide-based catalysts can strongly bond with the O atom of CO<sub>2</sub>, facilitating direct CO<sub>2</sub> dissociation. Sometimes, the unique CH<sub>4</sub> dissociation ability further inhibits CH<sub>4</sub> formation and improves the CO selectivity.

Based on this knowledge, active sites for tuning the CO adsorption and transformation are rationally designed. However, the local environments of the active sites are sometimes overlooked. The activation and diffusion of H<sub>2</sub>, which determine the hydrogenation of the carbon-containing

intermediates, could be controlled to optimize the reaction. Wang *et al.*<sup>19</sup> showed a representative example of tuning the selectivity of CO<sub>2</sub> hydrogenation *via* controlling H spillover around the metal nanoparticles. The Rh nanoparticles fixed within siliceous zeolite (Rh@S-1) enable high CO selectivity in CO<sub>2</sub> hydrogenation, which is beyond the general expectation of Rh-catalyzed CO<sub>2</sub> methanation (Fig. 10a–d). The referenced catalyst of Rh@HZSM-5 prefers to produce CH<sub>4</sub>, while both Rh@KZSM-5 (introducing K<sup>+</sup> by ion exchange) and Rh@S-1-OH (introducing silanol groups to the zeolite micropores) catalysts mainly give CH<sub>4</sub> at high CO<sub>2</sub> conversion. Because of the same content and size of Rh nanoparticles, these different catalytic performances are attributed to the nanoporous environment of zeolite sheaths. Experiments of a WO<sub>3</sub>-probe, H–D exchange and D<sub>2</sub>O treatment demonstrate that the stronger H spillover in the zeolite micropores with protons or silanols (Rh@HZSM-5 and Rh@S-1-OH) could provide active \*H species for deep hydrogenation, but studies on Rh@S-1 catalysts with weak hydrogen spillover ability are scarce (Fig. 10e–g).<sup>119–121</sup> In addition, the weakened CO adsorption on the S-1 zeolite fixed Rh nanoparticles also contributes to the hindered methanation in CO<sub>2</sub> hydrogenation.

It is also expected that investigations on the complete processes of the RWGS reaction and CO<sub>2</sub> methanation will help to elucidate the reaction mechanism of CO<sub>2</sub> hydrogenation, and guide the preparation and optimization of industrial catalysts. Compared with the simple products of CO and CH<sub>4</sub>, the synthesis of methanol and even C<sub>2+</sub> compounds with higher economic value is more desired. However, in practice, the inevitable CO or CH<sub>4</sub> formation in CO<sub>2</sub> hydrogenation will not only consumes hydrogen feed, but will also lead to insufficient



yield of target products. As a successful example, Yang *et al.*<sup>17</sup> reported ethanol synthesis from CO<sub>2</sub> hydrogenation over a Cu/Co<sub>3</sub>O<sub>4</sub> catalyst at high pressure (1–30 bar). These achievements expand the applications of the model reactions (RWGS and CO<sub>2</sub> methanation) to CO<sub>2</sub>-to-valuable chemical processes, offering good opportunities for industrial applications in the future, particularly in carbon neutralization for global environmental protection.

## Author contributions

L. W. and F.-S. X. conceived the topic and structure of the article. All authors reviewed and contributed to this paper.

## Conflicts of interest

There are no conflicts to declare.

## Acknowledgements

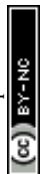
This work was supported by the National Natural Science Foundation of China (21932006 and 21822203).

## References

- Global Greenhouse Gas Reference Network, *Trends in Atmospheric Carbon Dioxide*, National Oceanic and Atmospheric Administration, Earth System Research Laboratory, Global Monitoring Division, U. S. Department of Commerce, Global, March 5, 2020.
- B. M. Tackett, E. Gomez and J. G. Chen, *Nat. Catal.*, 2019, **2**, 381–386.
- M. Mikkelsen, M. Jørgensen and F. C. Krebs, *Energy Environ. Sci.*, 2010, **3**, 43–81.
- M. Peters, B. Köhler, W. Kuckshinrichs, W. Leitner, P. Markewitz and T. E. Müller, *ChemSusChem*, 2011, **4**, 1216–1240.
- E. A. Quadrelli, G. Centi, J. L. Duplan and S. Perathoner, *ChemSusChem*, 2011, **4**, 1194–1215.
- M. Aresta, A. Dibenedetto and A. Angelini, *Chem. Rev.*, 2014, **114**, 1709–1742.
- M. D. Porosoff, B. Yan and J. G. Chen, *Energy Environ. Sci.*, 2016, **9**, 62–73.
- M. Aresta, A. Dibenedetto and E. Quaranta, *J. Catal.*, 2016, **343**, 2–45.
- S. Kattel, P. Liu and J. G. Chen, *J. Am. Chem. Soc.*, 2017, **139**, 9739–9754.
- W. Zhou, K. Cheng, J. Kang, C. Zhou, V. Subramanian, Q. Zhang and Y. Wang, *Chem. Soc. Rev.*, 2019, **48**, 3193–3228.
- X. Wang, H. Shi and J. Szanyi, *Nat. Commun.*, 2017, **8**, 513.
- J. C. Matsubu, V. N. Yang and P. Christopher, *J. Am. Chem. Soc.*, 2015, **137**, 3076–3084.
- J. C. Matsubu, S. Zhang, L. DeRita, N. S. Marinkovic, J. G. Chen, G. W. Graham, X. Pan and P. Christopher, *Nat. Chem.*, 2017, **9**, 120–127.
- S. Li, Y. Xu, Y. Chen, W. Li, L. Lin, M. Li, Y. Deng, X. Wang, B. Ge, C. Yang, S. Yao, J. Xie, Y. Li, X. Liu and D. Ma, *Angew. Chem., Int. Ed.*, 2017, **56**, 10761–10765.
- A. Aitbekova, L. Wu, C. J. Wrasman, A. Boubnov, A. S. Hoffman, E. D. Goodman, S. R. Bare and M. Cargnello, *J. Am. Chem. Soc.*, 2018, **140**, 13736–13745.
- S. Kattel, W. Yu, X. Yang, B. Yan, Y. Huang, W. Wan, P. Liu and J. G. Chen, *Angew. Chem., Int. Ed.*, 2016, **55**, 7968–7973.
- C. Yang, S. Liu, Y. Wang, J. Song, G. Wang, S. Wang, Z. J. Zhao, R. Mu and J. Gong, *Angew. Chem., Int. Ed.*, 2019, **58**, 11242–11247.
- M. D. Porosoff, X. Yang, J. A. Boscoboinik and J. G. Chen, *Angew. Chem., Int. Ed.*, 2014, **53**, 6705–6709.
- C. Wang, E. Guan, L. Wang, X. Chu, Z. Wu, J. Zhang, Z. Yang, Y. Jiang, L. Zhang, X. Meng, B. C. Gates and F.-S. Xiao, *J. Am. Chem. Soc.*, 2019, **141**, 8482–8488.
- L. X. Wang, E. Guan, Z. Wang, L. Wang, Z. Gong, Y. Cui, Z. Yang, C. Wang, J. Zhang, X. Meng, P. Hu, X. Q. Gong, B. C. Gates and F.-S. Xiao, *ACS Catal.*, 2020, **10**, 9261–9270.
- X. Zhang, S. Han, B. Zhu, G. Zhang, X. Li, Y. Gao, Z. Wu, B. Yang, Y. Liu, W. Baaziz, O. Ersen, M. Gu, J. T. Miller and W. Liu, *Nat. Catal.*, 2020, **3**, 411–417.
- L. Wang, W. Fang, L. Wang and F.-S. Xiao, *ChemSusChem*, 2020, **13**, 6300–6306.
- J. Cored, A. García-Ortiz, S. Ibora, M. J. Climent, L. Liu, C. H. Chuang, T. S. Chan, C. Escudero, P. Concepción and A. Corma, *J. Am. Chem. Soc.*, 2019, **141**, 19304–19311.
- A. Parastayev, V. Muravev, E. H. Osta, A. J. F. van Hoof, T. F. Kimpel, N. Kosinov and E. J. M. Hensen, *Nat. Catal.*, 2020, **3**, 526–533.
- F. Wang, S. He, H. Chen, B. Wang, L. Zheng, M. Wei, D. G. Evans and X. Duan, *J. Am. Chem. Soc.*, 2016, **138**, 6298–6305.
- Y. Yan, Y. Dai, H. He, Y. Yu and Y. Yang, *Appl. Catal., B*, 2016, **196**, 108–116.
- Y. Guo, S. Mei, K. Yuan, D. J. Wang, H. C. Liu, C. H. Yan and Y. W. Zhang, *ACS Catal.*, 2018, **8**, 6203–6215.
- J. Zhong, X. Yang, Z. Wu, B. Liang, Y. Huang and T. Zhang, *Chem. Soc. Rev.*, 2020, **49**, 1385–1413.
- X. Jiang, X. Nie, X. Guo, C. Song and J. G. Chen, *Chem. Rev.*, 2020, **120**, 7984–8034.
- F. Sha, Z. Han, S. Tang, J. Wang and C. Li, *ChemSusChem*, 2020, **13**, 6160–6181.
- S. Kuld, M. Thorhauge, H. Falsig, C. F. Elkjær, S. Helveg, I. Chorkendorff and J. Sehested, *Science*, 2016, **352**, 969–974.
- S. Kattel, P. J. Ramírez, J. G. Chen, J. A. Rodriguez and P. Liu, *Science*, 2017, **355**, 1296–1299.
- J. Graciani, K. Mudiyansele, F. Xu, A. E. Baber, J. Evans, S. D. Senanayake, D. J. Stacchiola, P. Liu, J. Hrbek, J. F. Sanz and J. A. Rodriguez, *Science*, 2014, **345**, 546–550.
- S. Kattel, B. Yan, Y. Yang, J. G. Chen and P. Liu, *J. Am. Chem. Soc.*, 2016, **138**, 12440–12450.
- F. Studt, I. Sharafutdinov, F. Abild-Pedersen, C. F. Elkjær, J. S. Hummelshøj, S. Dahl, I. Chorkendorff and J. K. Nørskov, *Nat. Chem.*, 2014, **6**, 320–324.



- 36 J. Wang, G. Li, Z. Li, C. Tang, Z. Feng, H. An, H. Liu, T. Liu and C. Li, *Sci. Adv.*, 2017, **3**, e1701290.
- 37 L. Wang, E. Guan, Y. Wang, L. Wang, Z. Gong, Y. Cui, X. Meng, B. C. Gates and F.-S. Xiao, *Nat. Commun.*, 2020, **11**, 1033.
- 38 D. Wang, Z. Xie, M. D. Porosoff and J. G. Chen, *Chem*, 2021, **7**, 2277–2311.
- 39 P. Gao, S. Dang, S. Li, X. Bu, Z. Liu, M. Qiu, C. Yang, H. Wang, L. Zhong, Y. Han, Q. Liu, W. Wei and Y. Sun, *ACS Catal.*, 2018, **8**, 571–578.
- 40 Z. Li, J. Wang, Y. Qu, H. Liu, C. Tang, S. Miao, Z. Feng, H. An and C. Li, *ACS Catal.*, 2017, **7**, 8544–8548.
- 41 M. K. Gnanamani, G. Jacobs, H. H. Hamdeh, W. D. Shafer, F. Liu, S. D. Hopps, G. A. Thomas and B. H. Davis, *ACS Catal.*, 2016, **6**, 913–927.
- 42 R. P. Ye, J. Ding, W. Gong, M. D. Argyle, Q. Zhong, Y. Wang, C. K. Russell, Z. Xu, A. G. Russell, Q. Li, M. Fan and Y. G. Yao, *Nat. Commun.*, 2019, **10**, 5698.
- 43 P. Gao, L. Zhang, S. Li, Z. Zhou and Y. Sun, *ACS Cent. Sci.*, 2020, **6**, 1657–1670.
- 44 J. Wei, Q. Ge, R. Yao, Z. Wen, C. Fang, L. Guo, H. Xu and J. Sun, *Nat. Commun.*, 2017, **8**, 15174.
- 45 J. Wei, R. Yao, Q. Ge, Z. Wen, X. Ji, C. Fang, J. Zhang, H. Xu and J. Sun, *ACS Catal.*, 2018, **8**, 9958–9967.
- 46 Z. He, M. Cui, Q. Qian, J. Zhang, H. Liu and B. Han, *Proc. Natl. Acad. Sci. U. S. A.*, 2019, **116**, 12654–12659.
- 47 Z. Li, Y. Qu, J. Wang, H. Liu, M. Li, S. Miao and C. Li, *Joule*, 2019, **3**, 570–583.
- 48 Y. Ni, Z. Chen, Y. Fu, Y. Liu, W. Zhu and Z. Liu, *Nat. Commun.*, 2018, **9**, 3457.
- 49 Y. Wang, L. Tan, M. Tan, P. Zhang, Y. Fang, Y. Yoneyama, G. Yang and N. Tsubaki, *ACS Catal.*, 2019, **9**, 895–901.
- 50 X. Cui, P. Gao, S. Li, C. Yang, Z. Liu, H. Wang, L. Zhong and Y. Sun, *ACS Catal.*, 2019, **9**, 3866–3876.
- 51 C. Zhou, J. Shi, W. Zhou, K. Cheng, Q. Zhang, J. Kang and Y. Wang, *ACS Catal.*, 2020, **10**, 302–310.
- 52 D. Xu, Y. Wang, M. Ding, X. Hong, G. Liu and S. C. E. Tsang, *Chem*, 2020, **7**, 849–881.
- 53 Z. He, Q. Qian, J. Ma, Q. Meng, H. Zhou, J. Song, Z. Liu and B. Han, *Angew. Chem., Int. Ed.*, 2016, **55**, 737–741.
- 54 S. Bai, Q. Shao, P. Wang, Q. Dai, X. Wang and X. Huang, *J. Am. Chem. Soc.*, 2017, **139**, 6827–6830.
- 55 L. Wang, L. Wang, J. Zhang, X. Liu, W. Zhang, Q. Yang, J. Ma, X. Dong, S. J. Yoo, J. G. Kim, X. Meng and F.-S. Xiao, *Angew. Chem., Int. Ed.*, 2018, **57**, 6104–6108.
- 56 L. Wang, S. He, L. Wang, Y. Lei, X. Meng and F.-S. Xiao, *ACS Catal.*, 2019, **9**, 11335–11340.
- 57 D. Xu, M. Ding, X. Hong, G. Liu and S. C. E. Tsang, *ACS Catal.*, 2020, **10**, 5250–5260.
- 58 L. Ding, T. Shi, J. Gu, Y. Cui, Z. Zhang, C. Yang, T. Chen, M. Lin, P. Wang, N. Xue, L. Peng, X. Guo, Y. Zhu, Z. Chen and W. Ding, *Chem*, 2020, **6**, 2673–2689.
- 59 Q. Zhang, J. Kang and Y. Wang, *ChemCatChem*, 2010, **2**, 1030–1058.
- 60 H. T. Luk, C. Mondelli, D. C. Ferré, J. A. Stewart and J. Pérez-Ramírez, *Chem. Soc. Rev.*, 2017, **46**, 1358–1426.
- 61 Y. Chen, J. Wei, M. S. Duyar, V. V. Ordonsky, A. Y. Khodakov and J. Liu, *Chem. Soc. Rev.*, 2021, **50**, 2337–2366.
- 62 S. Kasipandi and J. W. Bae, *Adv. Mater.*, 2019, **31**, 1803390.
- 63 C. Vogt, E. Groeneveld, G. Kamsma, M. Nachtegaal, L. Lu, C. J. Kiely, P. H. Berben, F. Meirer and B. M. Weckhuysen, *Nat. Catal.*, 2018, **1**, 127–134.
- 64 M. Xu, S. He, H. Chen, G. Cui, L. Zheng, B. Wang and M. Wei, *ACS Catal.*, 2017, **7**, 7600–7609.
- 65 J. Bao, G. Yang, Y. Yoneyama and N. Tsubaki, *ACS Catal.*, 2019, **9**, 3026–3053.
- 66 W. Li, H. Wang, X. Jiang, J. Zhu, Z. Liu, X. Guo and C. Song, *RSC Adv.*, 2018, **8**, 7651–7669.
- 67 Y. Lin, T. Zhu, X. Pan and X. Bao, *Catal. Sci. Technol.*, 2017, **7**, 2813–2818.
- 68 J. Xu, X. Su, H. Duan, B. Hou, Q. Lin, X. Liu, X. Pan, G. Pei, H. Geng, Y. Huang and T. Zhang, *J. Catal.*, 2016, **333**, 227–237.
- 69 W. Li, G. Zhang, X. Jiang, Yi. Liu, J. Zhu, F. Ding, Z. Liu, X. Guo and C. Song, *ACS Catal.*, 2019, **9**, 2739–2751.
- 70 S. Kattel, B. Yan, J. G. Chen and P. Liu, *J. Catal.*, 2016, **343**, 115–126.
- 71 Y. Yang, M. G. White and P. Liu, *J. Phys. Chem. C*, 2012, **116**, 248–256.
- 72 J. Wang, C. Y. Liu, T. P. Senftle, J. Zhu, G. Zhang, X. Guo and C. Song, *ACS Catal.*, 2020, **10**, 3264–3273.
- 73 A. Posada-Borbón and H. Grönbeck, *Phys. Chem. Chem. Phys.*, 2019, **21**, 21698–21708.
- 74 O. Martín, A. J. Martín, C. Mondelli, S. Mitchell, T. F. Segawa, R. Hauert, C. Drouilly, D. Curulla-Ferré and J. Pérez-Ramírez, *Angew. Chem., Int. Ed.*, 2016, **55**, 6261–6265.
- 75 N. Rui, Z. Wang, K. Sun, J. Ye, Q. Ge and C. Liu, *Appl. Catal., B*, 2017, **218**, 488–497.
- 76 J. Ye, C. Liu, D. Mei and Q. Ge, *ACS Catal.*, 2013, **3**, 1296–1306.
- 77 S. J. Tauster, S. C. Fung and R. L. Garten, *J. Am. Chem. Soc.*, 1978, **100**, 170–175.
- 78 S. J. Tauster, *Acc. Chem. Res.*, 1987, **20**, 389–394.
- 79 Y. Zhou, C. Jin, Y. Li and W. Shen, *Nano Today*, 2018, **20**, 101–120.
- 80 L. Wang, L. Wang, X. Meng and F.-S. Xiao, *Adv. Mater.*, 2019, **31**, 1901905.
- 81 J. Zhang, H. Wang, L. Wang, S. Ali, C. Wang, L. Wang, X. Meng, B. Li, D. S. Su and F.-S. Xiao, *J. Am. Chem. Soc.*, 2019, **141**, 2975–2983.
- 82 M. E. Strayer, J. M. Binz, M. Tanase, S. M. K. Shahri, R. Sharma, R. M. Rioux and T. E. Mallouk, *J. Am. Chem. Soc.*, 2014, **136**, 5687–5696.
- 83 M. Xu, S. Yao, D. Rao, Y. Niu, N. Liu, M. Peng, P. Zhai, Y. Man, L. Zheng, B. Wang, B. Zhang, D. Ma and M. Wei, *J. Am. Chem. Soc.*, 2018, **140**, 11241–11251.
- 84 H. Tang, Y. Su, B. Zhang, A. F. Lee, M. A. Isaacs, K. Wilson, L. Li, Y. Ren, J. Huang, M. Haruta, B. Qiao, X. Liu, C. Jin, D. Su, J. Wang and T. Zhang, *Sci. Adv.*, 2017, **3**, e1700231.
- 85 X. Li, J. Lin, L. Li, Y. Huang, X. Pan, S. E. Collins, Y. Ren, Y. Su, L. Kang, X. Liu, Y. Zhou, H. Wang, A. Wang,



- B. Qiao, X. Wang and T. Zhang, *Angew. Chem., Int. Ed.*, 2020, **59**, 19983–19989.
- 86 Y. Zhang, Z. Zhang, X. Yang, R. Wang, H. Duan, Z. Shen, L. Li, Y. Su, R. Yang, Y. Zhang, X. Su, Y. Huang and T. Zhang, *Green Chem.*, 2020, **22**, 6855–6861.
- 87 Y. Guo, Z. Liu, F. Zhang, D. Wang, K. Yuan, L. Huang, H. C. Liu, S. D. Senanayake, J. A. Rodriguez, C. H. Yan and Y. W. Zhang, *ChemCatChem*, 2021, **13**, 874–881.
- 88 X. Chen, X. Su, H. Y. Su, X. Liu, S. Miao, Y. Zhao, K. Sun, Y. Huang and T. Zhang, *ACS Catal.*, 2017, **7**, 4613–4620.
- 89 F. J. C. M. Toolenaar, A. G. T. M. Bastein and V. Ponec, *J. Catal.*, 1983, **82**, 35–44.
- 90 D. A. Panayotov and J. T. Yates, *J. Phys. Chem. C*, 2007, **111**, 2959–2964.
- 91 D. A. Panayotov and J. T. Yates, *Chem. Phys. Lett.*, 2007, **436**, 204–208.
- 92 M. Bowker, P. Stone, P. Morrall, P. Smith, R. Smith, R. Bennett, N. Perkins, R. Kwon, C. Pang, E. Fourre and M. Hall, *J. Catal.*, 2005, **234**, 172–181.
- 93 S. Zhang, P. N. Plessow, J. J. Willis, S. Dai, M. Xu, G. W. Graham, M. Cargnello, F. Abild-Pedersen and X. Pan, *Nano Lett.*, 2016, **16**, 4528–4534.
- 94 H. Tang, F. Liu, J. Wei, B. Qiao, K. Zhao, Y. Su, C. Jin, L. Li, J. Liu, J. Wang and T. Zhang, *Angew. Chem., Int. Ed.*, 2016, **55**, 10606–10611.
- 95 H. Tang, J. Wei, F. Liu, B. Qiao, X. Pan, L. Li, J. Liu, J. Wang and T. Zhang, *J. Am. Chem. Soc.*, 2016, **138**, 56–59.
- 96 H. Tang, Y. Su, Y. Guo, L. Zhang, T. Li, K. Zang, F. Liu, L. Li, J. Luo, B. Qiao and J. Wang, *Chem. Sci.*, 2018, **9**, 6679–6684.
- 97 C. Yang and C. W. Garland, *J. Phys. Chem.*, 1957, **61**, 1504–1512.
- 98 J. T. Yates, T. M. Duncan, S. D. Worley and R. W. Vaughan, *J. Chem. Phys.*, 1979, **70**, 1219.
- 99 F. Calle-Vallejo, J. Tymoczko, V. Colic, Q. H. Vu, M. D. Pohl, K. Morgenstern, D. Loffreda, P. Sautet, W. Schuhmann and A. S. Bandarenka, *Science*, 2015, **350**, 185–189.
- 100 J. K. Nørskov, T. Bligaard, J. Rossmeisl and C. H. Christensen, *Nat. Chem.*, 2009, **1**, 37–46.
- 101 B. Yan, B. Zhao, S. Kattel, Q. Wu, S. Yao, D. Su and J. G. Chen, *J. Catal.*, 2019, **374**, 60–71.
- 102 N. Nityashree, C. A. H. Price, L. Pastor-Perez, G. V. Manohara, S. Garcia, M. M. Maroto-Valer and T. R. Reina, *Appl. Catal., B*, 2020, **261**, 118241.
- 103 P. Liu and J. A. Rodriguez, *J. Chem. Phys.*, 2004, **120**, 5414–5423.
- 104 J. G. Chen, *Chem. Rev.*, 1996, **96**, 1477–1498.
- 105 A. Zhang, A. Zhu, B. Chen, S. Zhang, C. Au and C. Shi, *Catal. Commun.*, 2011, **12**, 803–807.
- 106 S. Yao, X. Zhang, W. Zhou, R. Gao, W. Xu, Y. Ye, L. Lin, X. Wen, P. Liu, B. Chen, E. Crumlin, J. Guo, Z. Zuo, W. Li, J. Xie, L. Lu, C. J. Kiely, L. Gu, C. Shi, J. A. Rodriguez and D. Ma, *Science*, 2017, **357**, 389–393.
- 107 Z. Li, Y. Cui, Z. Wu, C. Milligan, L. Zhou, G. Mitchell, B. Xu, E. Shi, J. T. Miller, F. H. Ribeiro and Y. Wu, *Nat. Catal.*, 2018, **1**, 349–355.
- 108 J. Dong, Q. Fu, Z. Jiang, B. Mei and X. Bao, *J. Am. Chem. Soc.*, 2018, **140**, 13808–13816.
- 109 X. Zhang, X. Zhu, L. Lin, S. Yao, M. Zhang, X. Liu, X. Wang, Y. W. Li, C. Shi and D. Ma, *ACS Catal.*, 2017, **7**, 912–918.
- 110 X. Zhang, Y. Liu, M. Zhang, T. Yu, B. Chen, Y. Xu, M. Crocker, X. Zhu, Y. Zhu, R. Wang, D. Xiao, M. Bi, D. Ma and C. Shi, *Chem*, 2020, **6**, 3312–3328.
- 111 P. Chen, G. Zhao, X. R. Shi, J. Zhu, J. Ding and Y. Lu, *iScience*, 2019, **17**, 315–324.
- 112 T. S. Galhardo, A. H. Braga, B. H. Arpini, J. Szanyi, R. V. Gonçalves, B. F. Zornio, C. R. Miranda and L. M. Rossi, *J. Am. Chem. Soc.*, 2021, **143**, 4268–4280.
- 113 X. Deng, A. Verdaguer, T. Herranz, C. Weis, H. Bluhm and M. Salmeron, *Langmuir*, 2008, **24**, 9474–9478.
- 114 S. Izhar, H. Kanetsugi, H. Tominaga and M. Nagai, *Appl. Catal., A*, 2007, **317**, 82–90.
- 115 L. Dietz, S. Piccinin and M. Maestri, *J. Phys. Chem. C*, 2015, **119**, 4959–4966.
- 116 L. Wang, Y. Yi, H. Guo and X. Tu, *ACS Catal.*, 2018, **8**, 90–100.
- 117 L. Liu, Z. Zhang, S. Das and S. Kawi, *Appl. Catal., B*, 2019, **250**, 250–272.
- 118 C. Mirodatos, J. A. Dalmon and G. A. Martin, *Stud. Surf. Sci. Catal.*, 1984, **19**, 505–512.
- 119 R. Prins, *Chem. Rev.*, 2012, **112**, 2714–2738.
- 120 J. Im, H. Shin, H. Jang, H. Kim and M. Choi, *Nat. Commun.*, 2014, **5**, 3370.
- 121 W. Karim, C. Spreafico, A. Kleibert, J. Gobrecht, J. VandeVondele, Y. Ekinici and J. A. van Bokhoven, *Nature*, 2017, **541**, 68–71.

